Improving the sensitivity of Astronomical Curvature Wavefront Sensor using dual-stroke curvature

Olivier Guyon, Celia Blain, Hideki Takami, Yutaka Hayano, Masayuki Hattori, Makoto Watanabe
Subaru Telescope, 650 N. A'ohoku Place, Hilo, 96720 HI, USA
`guyon@naoj.org`

ABSTRACT

Curvature wavefront sensors measure wavefront phase aberration by acquiring two intensity images on either side of the pupil plane. Low order Adaptive Optics (AO) systems using Curvature Wavefront Sensing (CWFS) have proved to be highly efficient for astronomical applications: they are more sensitive, use fewer detector elements, and achieve, for the same number of actuators, higher Strehl ratios than AO systems using more traditional Shack-Hartmann wavefront sensors. In higher order systems, however, curvature wavefront sensors loose sensitivity to low spatial frequencies wavefront aberrations. This effect, often described as "noise propagation", limits the usefulness of curvature wavefront sensing for high order AO systems and/or large telescopes. In this paper, we first explain how this noise propagation effect occurs and then show that this limitation can be overcome by acquiring four defocused images of the pupil instead of two. This solution can be implemented without significant technology development and can run with a simple linear wavefront reconstruction algorithm at $>$ kHz speed. We have successfully demonstrated in the laboratory that the four conjugation planes can be sequentially obtained at $>$ kHz speed using a speaker/vibrating membrane assembly commonly used in current curvature AO systems. Closed loop simulation show that implementing this scheme is equivalent to making the guide star 1 to 1.5 magnitude brighter for the configuration tested (188 actuator elements on 8m telescope). Higher sensitivity gains are expected on curvature systems with higher number of actuators.

Subject headings: instrumentation: adaptive optics — techniques: high angular resolution

1. Introduction

Adaptive optics (AO) systems use a Wavefront Sensor (WFS) to measure the phase (and sometimes amplitude) corrugations of the incoming wavefront. This signal is then used to drive a deformable mirror (DM) to cancel these phase errors.

While DM technology, computing power and detector performances are continuously improving, wavefront sensing accuracy is ultimately limited by the available number of photons and the speed of the atmospheric turbulence. Using a WFS technique which offers high sensitivity is therefore critical for both general astrophysics (where the guide star is usually faint, and, consequently, most systems are photon-starved), and for high contrast imaging with an "Extreme-AO" system (where the large number of element/short sampling time makes the system photon-starved even on bright sources).

Most high-order AO systems are designed around a Shack-Hartmann WFS (SHWFS): wavefront slopes are measured in front of individual subapertures. This wavefront sensing scheme is often favored for its robustness: it can measure wavefronts with large errors and performs well on extended targets (such as a laser guide star).

Adaptive Optics systems using Curvature Wavefront Sensing (CWFS) (Roddier 1988) are less common, but have been very successful (Roddier 1998; Racine 2006), especially for faint guide stars. They offer several key advantages:

- Efficient use of number of detectors: one detector per subaperture only, as opposed to at least 4 for a SHWFS.
- Their optical gain (which quantifies how phase aberrations are transformed into intensity signal by the WFS) can be tuned "on-the-fly" by changing the vibrating membrane stroke (the equivalent in SHWFS would be to be able to change subaperture size)
- CWFS benefit from the AO correction upstream. They become more efficient as the wavefront is cleaner because this allows larger membrane strokes to be used. CWFS is therefore attractive for high Strehl AO.

In its conventional implementation, CWFS however suffers from serious limitations which makes it a non-ideal choice for future high-order AO systems. These limitations are reviewed and quantified in §2. We then show in §3 that they can be overcome by utilizing four conjugation planes instead of two. A simple linear control loop, described in §5 can take advantage of the improved sensitivity offered by using four conjugation altitudes.

2. Conventional CWFS and its limitations

2.1. Curvature Measurement and Wavefront Fresnel Propagation

In a CWFS, light intensity is alternatively measured in planes optically conjugated on either side of the telescope pupil (Roddier 1991). We note that these two planes can also be assumed to be on either side of the focal plane: both representations are equivalent, as a "defocused" pupil image is also a defocused focal plane image. A vibrating membrane (VM), which acts as a variable focal length element in the focal plane, is used to quickly alternate between these two planes on the detector array. We denote D the telescope diameter, f_1 the focal length of the beam delivered to the VM, and f_m the VM's focal length. The detector array is conjugated to the telescope pupil for a flat VM ($f_m = \infty$). We denote z the distance from the telescope pupil to the plane conjugated to the detector array:

$$z = -\frac{{f_1}^2}{f_m}. \tag{1}$$

In current visible CWFSs, z alternates between z_+ and z_-, with $z_+ = -z_- \approx 500 - 1500km$. For example, on the Subaru AO36 system (Takami et al. 2004), this distance is obtained with $f_m \approx \pm 0.2 - 0.5m$ and $f_1 = 528m$ (F/66 beam on a 8m telescope).

We now show how an OPD aberration at a given spatial frequency is transformed into an intensity signal in a curvature wavefront sensor. CWFSs rely on Fresnel propagation over the distance z to transform phase aberrations into intensity fluctuations. We denote $W(\vec{u}, z)$ the complex amplitude, where $\vec{u}$ is the 2D coordinate on a plane perpendicular to the optical axis and z is the coordinate along the optical axis. A pupil plane OPD aberration of spatial frequency $\vec{f}$, spatial phase θ and amplitude h (peak OPD), corresponding to the complex amplitude:

$$W(\vec{u}, 0) = \exp\left(i\frac{2\pi h}{\lambda}\sin(2\pi\vec{u}\vec{f} + \theta)\right) \tag{2}$$

is transformed, after propagation over z, into

$$W(\vec{u}, z) = \exp\left(e^{id\phi} \times i\frac{2\pi h}{\lambda}\sin(2\pi\vec{u}\vec{f} + \theta)\right) \tag{3}$$

where

$$d\phi = \pi|\vec{f}|^2 z\lambda. \tag{4}$$

$d\phi$ quantifies how the OPD aberration (phase only) is transformed in a combination of phase and amplitude by Fresnel propagation. If the propagation distance z is such that $d\phi = \pi/2$, $W(\vec{u}, z)$ is real: Fresnel propagation has transformed the phase aberration into a pure intensity aberration without phase. If $d\phi$ is a multiple of 2π, the propagated OPD aberration is a copy of the original OPD aberration without any amplitude signal (this is the Talbot effect).

The contrast between the defocused images $W_+ = |W(\vec{u}, z_+)|^2$ and $W_- = |W(\vec{u}, z_-)|^2$ is :

$$C = \frac{W_+ - W_-}{W_+ + W_-} = \tanh\left(2\sin(d\phi)\frac{2\pi h}{\lambda}\sin(2\pi\vec{u}\vec{f} + \theta)\right) \tag{5}$$

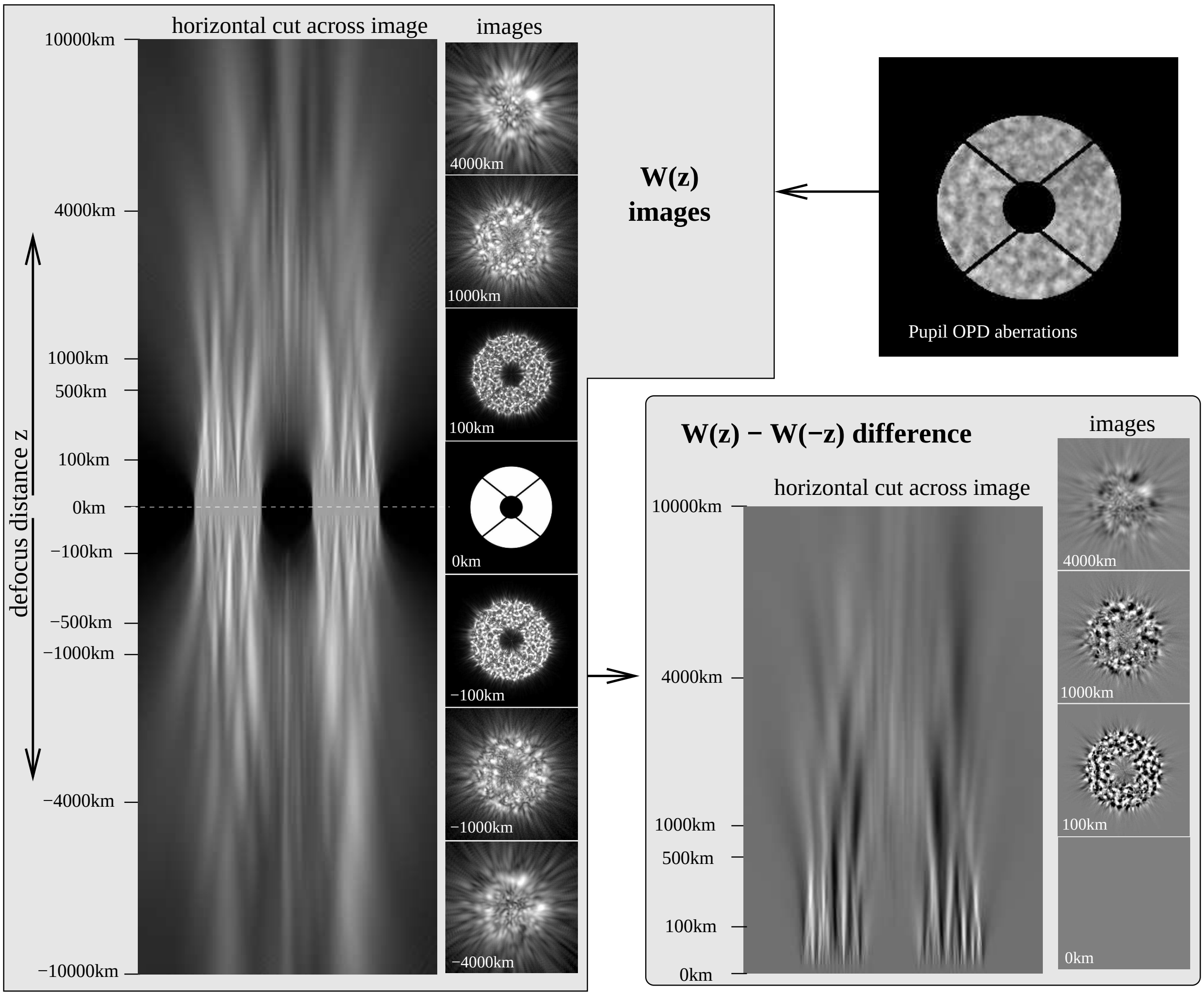

Fig. 1.— Measurement in a CWFS. The pupil optical pathlength difference (OPD) aberrations (upper right) are transformed into intensity fluctuations (left) by Fresnel propagation over a distance z. The difference between pairs of images ($W(z)$,$W(-z)$) obtained on either size of the pupil plane yields the OPD curvature (lower right). All simulations used to produce this figure assume a $0.4 - 0.8\mu$m bandpass.

The steps described above, which transform phase aberrations into intensity modulations, are illustrated in Figure 1, where the OPD aberration introduced in the pupil is transformed in intensity variations by Fresnel propagation on either side of the pupil. To better illustrate this process, Figure 2 shows how a single spatial frequency OPD aberration creates intensity modulations in a curvature WFS: in this second figure, only the difference $W(z) - W(-z)$ between the two symmetrically defocused pupil images is shown. Both figures show that high spatial frequencies are most easily visible in planes conjugated close to the pupil plane, while low spatial frequencies are most obvious when looking further away from the pupil plane.

Figure 2 can be directly related to equations 3, 4 and 5: in the example shown in the left (2 m period aberration), $d\phi = \pi/2$ for $z \approx 3000km$ and this is the conjugation altitude where the signal is the strongest. At higher spatial frequencies (Figure 2, right), $d\phi = \pi/2$ closer to the pupil plane. For spatial frequencies within the control of the AO system, $d\phi$ is usually kept small: $d\phi < 1$ and $4\pi h \sin(d\phi)/\lambda < 1$, and equation 5 becomes

$$C \approx 4\pi^2 f^2 z h \sin(2\pi \vec{u}\vec{f} + \theta). \qquad (6)$$

Comparison with equation 2 shows that under this approximation, C is achromatic and proportional to the second derivative (curvature) of the wavefront's OPD, as shown by the f^2 term in front of $\sin(2\pi\vec{u}\vec{f} + \theta)$. This is the standard mode of operation of CWFSs, which, coupled with a curvature-driven DM, allows efficient correction with a quasi-diagonal system response matrix.

2.2. Optimal defocus distance

As shown by equations 5 and 6, increasing the defocus distance z to approach $d\phi = \pi/2$ improves the wavefront sensing sensitivity by increasing the contrast signal. With larger values of z, the conversion from phase to intensity performed by the wavefront sensor is more efficient: z acts as an "optical gain" in the CWFS, and should therefore be chosen large. There are however limits to how much z can be increased, which are reviewed in this section. These limits are key to understanding the limitations of current curvature-based AO systems.

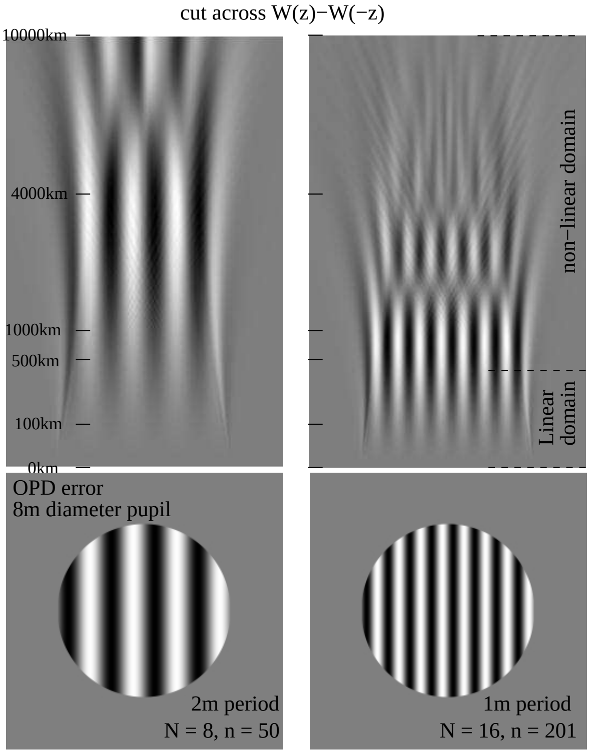

Fig. 2.— Wavefront aberration (bottom) and corresponding signal (top) measured by a polychromatic (0.4 μm - 0.8 μm) CWFS for respectively a low (left) and a high (right) spatial frequency. The optimal defocus distance, at which the measured signal (top) is strongest, is larger for lower spatial frequencies. For the high spatial frequency case (right), the linearity domain, within which the signal measured is proportional to both the defocus distance and the strength of the aberration, extends to approximately $500km$.

We denote N the linear number of sensing elements (usually approximately equal to the number of actuators on the DM) across the telescope diameter D: the total number of elements is $n = \pi N^2/4$. The maximum spatial frequency seen by the system is $N/2D$.

2.2.1. System linearity

Conventional operation of a curvature AO system relies on the linearity of the WFS measurement: the contrast C should be proportional to the geometric curvature of the wavefront, as shown in equation 6. Therefore, the approximation $\sin(d\phi) \approx d\phi$ must be valid and $4\pi h \sin(d\phi)/\lambda$ must be less than 1. We note that in closed loop, $2\pi h/\lambda$ is usually less than 1: even though the overall wavefront quality may be worse than 1 λ RMS, a single spatial frequency carries only a fraction of the overall wavefront aberration. If $d\phi < \pi$, then we can also assume that $4\pi h \sin(d\phi)/\lambda < 1$.

If the $d\phi << \pi$ constraint is not satisfied, then the WFSs signal is no longer linear: equation 6 is no longer valid. In the extreme case, if $d\phi > \pi$, $\sin(d\phi)$ and $d\phi$ can have opposite signs, in which case the CWFS will produce a curvature signal with a sign opposite to the actual wavefront curvature: adopting equation 6 would then lead to runaway amplification of high spatial frequencies in a closed loop control. As shown in equ. 4 and Figure 2, this effect occurs at a defocus distance which is smaller for higher spatial frequencies.

In a curvature AO system, $d\phi$ must therefore be less than π at the highest spatial frequency seen by the WFS, and z must therefore be small compared to:

$$z_1 = \frac{4D^2}{N^2\lambda}. \quad (7)$$

2.2.2. *Residual wavefront aberrations in the wavefront sensor*

In a CWFS, high and low order aberrations are strongly coupled: a large residual in a low order mode prevents accurate sensing of high order modes. A Tilt residual angle α introduces a αz shift of the defocused pupil image. This spatial shift must be less than about $\pi/2$ (π from z_+ to z_-) at the highest spatial frequency corrected by the system: otherwise, these frequencies will be amplified rather than corrected. z must therefore be small compared to z_2, with:

$$z_2 = \frac{D}{2\alpha N}. \quad (8)$$

The above equation ensures that for a given tilt, the defocus distance is kept small enough to avoid displacing the intensity signal by more than a resolution element in the sensor. The effect of a tilt on the wavefront measurement of a single spatial frequency is shown in Figure 3. In this example, the aberration is best measured at 500km defocus distance without tilt, but the signal almost vanishes at this altitude with tilt.

Likewise, high spatial frequencies in the pupil will blur the out-of-pupil-plane images. The blurring size is simply equal to the defocus distance from the pupil multiplied by the instantaneous size of the point spread function (PSF) in the visible wavefront sensor. In equation 8, α should therefore be the half-width of the visible PSF, not just the amplitude of the tip-tilt residual. Unless the number of actuators in the AO system is sufficient to significantly improve the visible PSF, a residual tilt angle $\alpha \approx 100mas$ is probably a realistic figure under good atmospheric conditions (this is the value adopted for table 1).

This behavior is indeed commonly observed on current AO systems, where the membrane stroke / defocus distance has to be reduced as α increases because of a faint guide star and/or bad seeing.

We note that uncorrected atmospheric dispersion (or actual angular extend of the source) has a similar effect and will prevent z from exceeding z_3, with

$$z_3 = \frac{2D}{\alpha_{AD} N} \quad (9)$$

where α_{AD} is the atmospheric dispersion across the spectral bandwidth (or the angular size of the source). In table 1, $\alpha_{AD} = 0.5''$ is assumed (corresponding to 45 deg elevation with a 0.5 μm – 0.9 μm band). Wavefront sensors equipped with an Atmospheric Dispersion Compensator (ADC) do not suffer from this limitation.

2.3. Discussion

Table 1 compares values of z_1, z_2 and z_3 to actual defocus distances used for 3 existing curvature AO systems: PUEO on the Canada-France-Hawaii telescope (Rigaut et al. 1998), AO36 on the Subaru telescope (Takami et al. 2004) and MACAO on the Very Large Telescope (Arsenault et al. 2004). Subaru's new AO188 system is also shown, with defocus values derived from simulations. An hypothetical 500-actuators "Extreme AO" curvature system is also listed. The same values are shown in Figure 4 along with the theoretical limits z_1 and z_2 discussed earlier.

Four approximate domains can be identified in this figure:

1. Low-order CWFS system: The number of actuators is insufficient to significantly improve the visible light PSF. z is kept close to

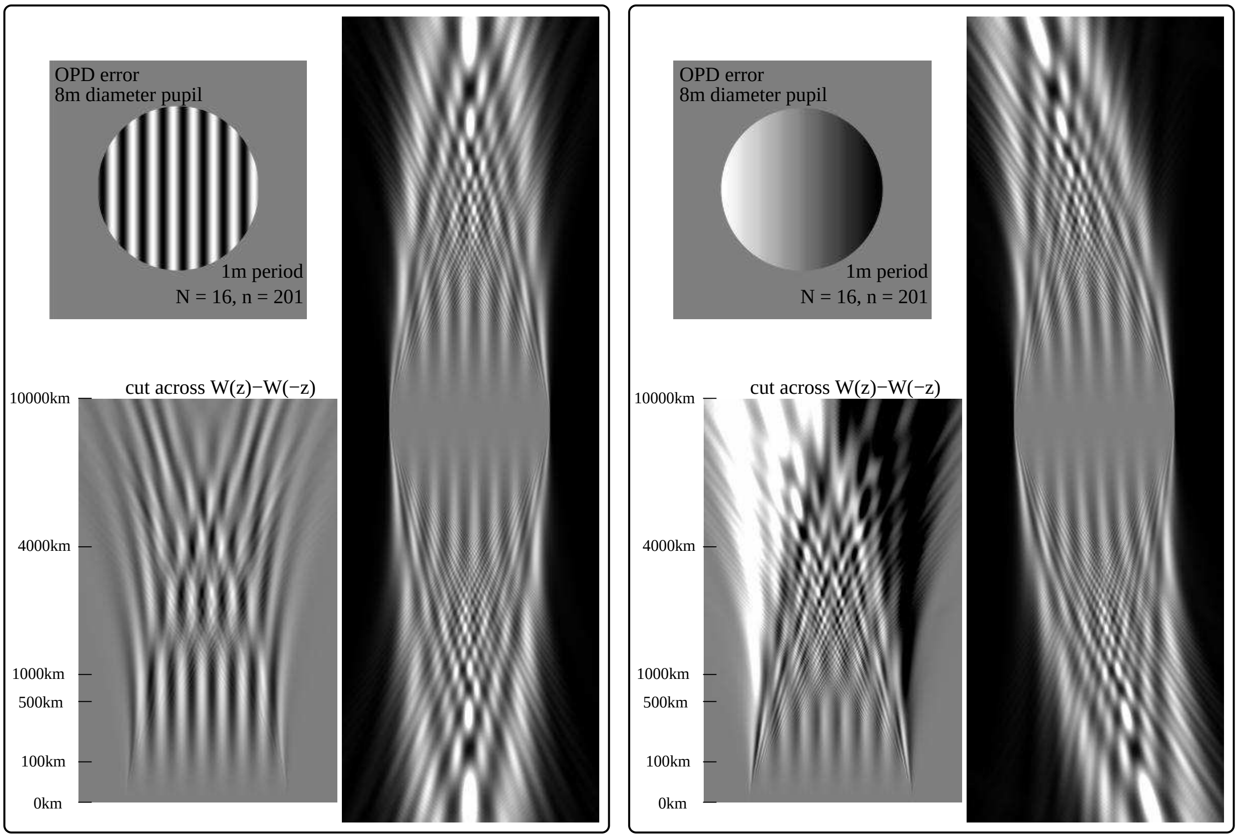

Fig. 3.— Monochromatic ($\lambda = 0.7\mu m$) curvature wavefront measurement of a 1m period OPD aberration without (left) and with (right) tip-tilt. In each case, the OPD aberration (upper left), a cut of intensity distribution from -10 000 km to 10 000 km (right, non-linear scale in altitude), and the $W(z) - W(-z)$ signal (bottom left) are shown.

$z_2(100mas)$. Most current CWFS-based AO systems belong to this class.

2. Mid-order CWFS system: The AO correction starts to improve the visible light PSF, and z_2 becomes in fact smaller than $z_2(100mas)$, allowing larger defocus distances to be used. In open loop systems, this would not occur, and z_2 would stay low.

3. High-order CWFS system: Actuators are smaller than r_0 and the defocus distance is equal to z_1. This defocus distance is still larger than would be allowed by natural seeing.

4. Very high order CWFS system: The size of the actuators is small enough for z_1 to be smaller than z_2. Wavefront correction does not enable higher defocus distance.

This simple qualitative model illustrates that as the number of actuators increases, the defocus distance inexorably shrinks, and sensing of low order aberrations becomes increasingly inefficient ($d\phi$ is much smaller than $\pi/2$). For low order CWFS systems, the defocus distance decreases very rapidly with increasing number of actuators - in most cases, this rapid drop in sensitivity is however more than offset by the benefit of having a larger number of actuators. In the "Mid-order" domain, the WFS benefits from AO correction and the speed at which defocus distance drops is greatly slowed down: the benefit of having more actuators still outweights the penalty of shorter defocus distance. However, once the actuator size

Table 1

AO system examples

system	λ	ADC	n	N	D	z used	z_1	$z_2(100mas)$	z_3
PUEO	0.7 μm	no	19	4.92	3.6	470km – 930km	3060km	755km	604km
AO36	0.7 μm	no	36	6.77	8.0	641km – 1500km	7980km	1220km	975km
MACAO	0.7 μm	no	60	8.74	8.0	315km – 1600km	4788km	944km	755km
AO188	0.7 μm	yes	188	15.47	8.0	≈1000km (simulation)	1528km	533km	(426km)
ExAO500	0.7 μm	yes	500	25.23	8.0	≈400km ?	574km	327km	(261km)

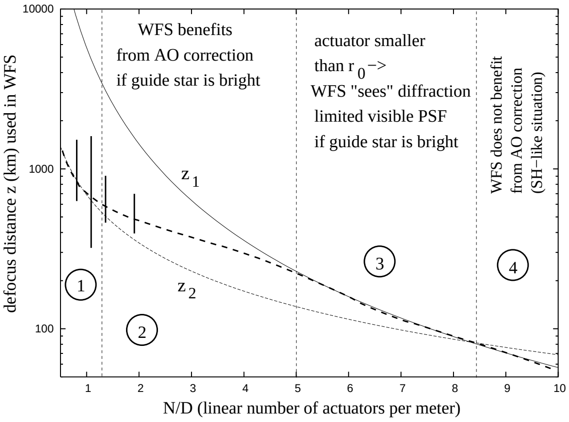

Fig. 4.— Defocus values used on curvature AO systems listed in table 1 (shown as vertical bars), compared with z_1 and z_2. The approximate evolution of defocus distance with actuator density is shown as a dashed line and discussed in the text. This figure assumes a very bright guide star.

becomes comparable to r_0, defocus distance drops more rapidly again, and the larger number of actuators is only beneficial for very bright guide stars.

The ability of a CWFS to efficiently sense low order aberration decreases as the actuator density increases. This effect has an especially strong negative impact on the performance of mid and high-order CWFS systems: as the guide star becomes fainter, the corrected wavefront degrades, which in turn reduces the defocus distance, and therefore further reduces the sensitivity to sense low order modes.

3. Linear Dual Stroke Curvature Wavefront Sensing: Principle

We have shown in §2 that in conventional CWFS, increasing the number of actuators reduces the measurement sensitivity for low order aberrations. A painful compromise therefore needs to be found between two opposite requirements: a high number of actuators is necessary to achieve high Strehl ratios on bright stars, and a low number of actuators is essential to maintain sensitivity for faint guide stars. For a given stellar brightness and atmospheric conditions, an optimal number of actuators therefore exists.

The fundamental problem of conventional CWFS is that it has to be either tuned for high order aberrations and bright targets (small defocus distance) or low order aberration and faint targets (large defocus distance), but cannot be simultaneously efficient at measuring both (Guyon 2005). This limitation is also often referred to as the "noise propagation" effect, which also affects, at a lesser degree, Shack-Hartmann WFS.

As illustrated in Figure 5, a solution to this limitation would be to include an additional large defocus CWFS within the AO system (we denote $dz2$ this new large defocus distance, and dz_1 the small defocus distance used in the other CWFS). This second sensor would be dedicated to the measurement of low order aberrations. Even though light needs to be divided between the two WFSs, the large gain in sensitivity for low order aberrations sensing outweights the loss of light available for high-order aberrations sensing. In a 50%/50% split between the two WFSs, the sensitivity gain for low order aberrations is equivalent to a factor $0.5 \times (dz_2/dz_1)^2$ gain in stellar brightness, while the loss for high order aberration is equivalent to reducing by half the number of photons. As shown in §5.2, dz_2/dz_1 is in most cases about 3.

In the next two sections, we look into the hardware and software implementation of a CWFS system with two defocus altitudes. We show that such a system can be obtained with relatively mi-

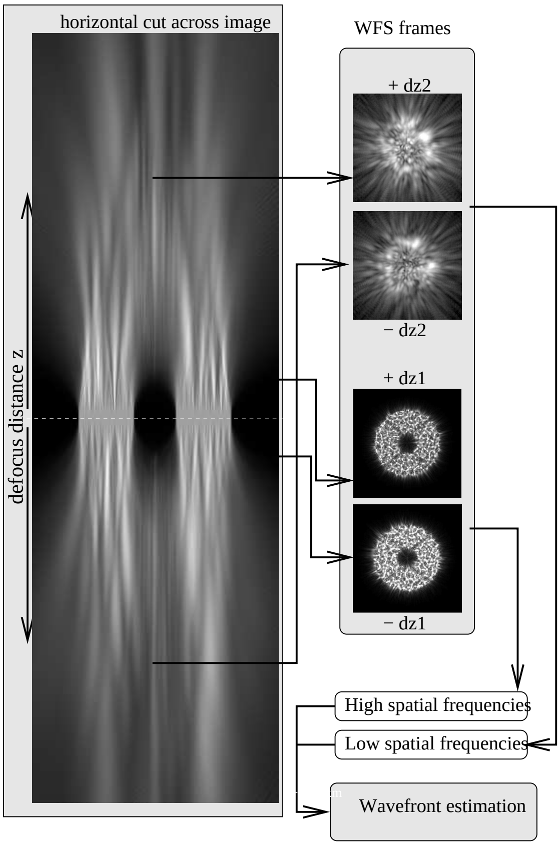

Fig. 5.— Principle of dual stroke curvature wavefront sensing. Four defocused pupil images are acquired by the wavefront sensor. The "small defocus" pair of images ($+/-dz_1$) are used to extract high spatial frequencies while the "large defocus" pair ($+/-dz_2$) encodes low spatial frequencies.

nor modifications to current conventional CWFS systems. To implement the CWFS system with two defocus distances, two main issues must be solved: (1) How to modify the hardware to achieve the two defocus distances ? (2) How does the AO control loop algorithm need to be modified in this improved sensing mode ?

4. Obtaining the desired defocus with a vibrating membrane mirror

In conventional CWFS systems, to rapidly alternate between defocus distances, a vibrating reflective membrane is used. A speaker produces acoustic waves at a single frequency, chosen to excite the membrane's fundamental vibration frequency. The membrane's vertical displacement excluding piston is to a good approximation $Ar^2 \sin(2\pi f t)$, where r is the distance from the membrane center, f and A are respectively the frequency and amplitude of the electric signal fed to the speaker. This WFS scheme must be modified to support our new wavefront sensing mode. Rather than explicitly building two distinct WFSs (one per defocus altitude), and inserting a beam splitter to divide light between them, we propose to drive the defocusing vibrating membrane to produce the four required conjugations ($+dz_1$, $-dz_1$, $+dz_2$ and $-dz_2$) on the same detector array. The membrane now vibrates with two different amplitudes (or strokes). This "dual stroke" option ensures that no additional hardware needs to be built, makes optimal use of a limited number of detectors, and offers maximum flexibility: switching between conventional single stroke and dual stroke, modifying the values of dz_1 or dz_2, and changing the photon allocation ratio between the two "virtual" WFSs can all be done by modifying the vibrating membrane motion. How exactly this is achieved is now detailed.

In dual stroke CWFS, we would like the membrane motion to be different than a sine wave: it should be a single period of a low amplitude (dz_1) sine wave immediately followed by a single period of a higher amplitude (dz_2) sine wave (the length of the two sine waves may be different if we wish to allocate more than 50% of the photons to one of the two "virtual WFSs"). This whole pattern is then to be repeated at ≈kHz frequency. Since the frequency response of the speaker/acoustic cavity assembly is not expected to be flat (see Figure 7, top left), controlling the membrane motion for a non-sine wave pattern is not as simple as sending the desired pattern directly to the speaker. Our dual stroke pattern is composed of many individual frequencies (its Fourier transform is no longer a single peak); each of these frequencies is amplified and phase shifted according to the frequency response (complex transfer function) of the speaker/acoustic cavity assembly.

To control the VM to produce arbitrary waveforms, we propose to use an iterative algorithm as shown in Figure 6. A laser beam and a position sensing device (PSD) are used to measure the real-time position of the membrane surface. The laser is pointed some distance off the center of the mem-

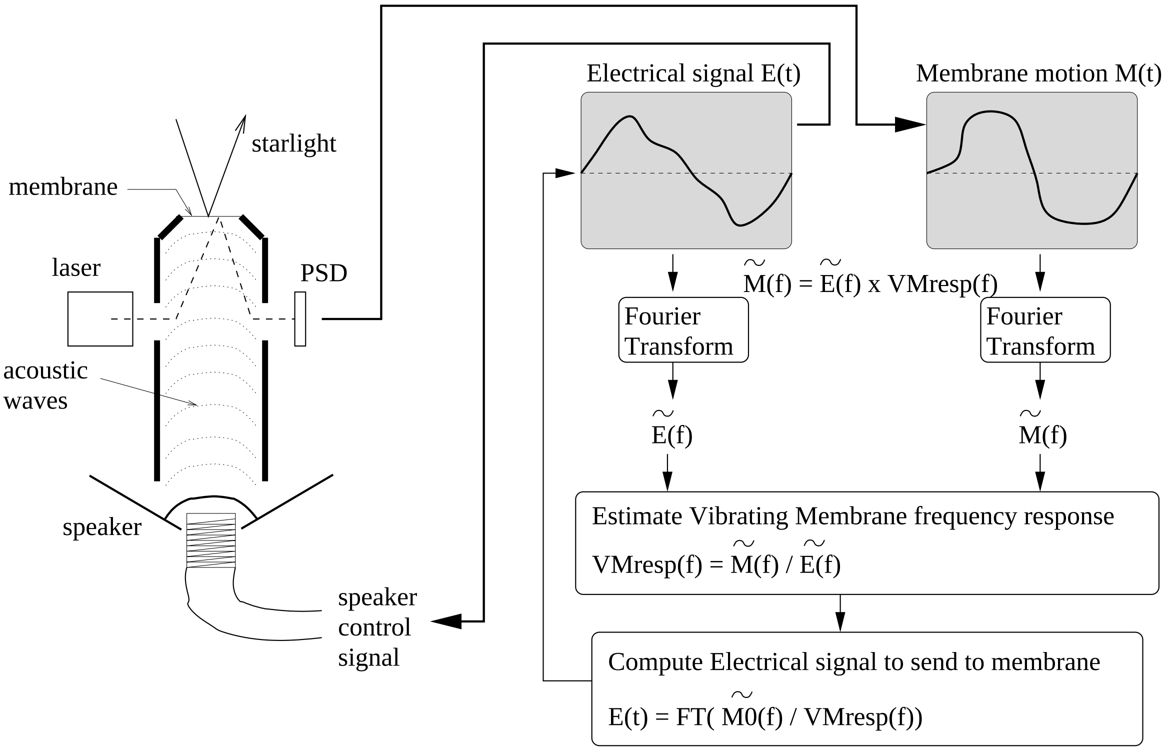

Fig. 6.— Closed loop control scheme for driving the Vibrating Membrane (VM) to produce arbitrary waveforms. The VM frequency response $VMresp(f)$ is constantly monitored by comparison of the electric signal sent to the speaker and the actual motion of the membrane (measured as a laser spot position on a Position Sensing Device - PSD). This frequency response is used to update the electrical signal, which is computed to produce the desired VM motion M0(t).

brane in order to measure the membrane curvature as a local slope which displaces the laser spot on the PSD. By using the backside of the membrane for this position sensing, we can ensure that laser light does not contaminate the precious starlight photons used for wavefront sensing. The discrepancy between the input electrical signal $E(t)$ and the output membrane displacement $M(t)$ is sufficient to recover the frequency response (both amplitude and phase) of the speaker/acoustic cavity assembly. This frequency response is then used to update $E(t)$ such that $M(t)$ matches the desired membrane motion.

We have implemented this scheme in the laboratory, with the only difference that we used the front side of the membrane for position sensing (this made the packaging easier). The membrane position was sampled at 100 kHz with a HeNe laser. Results, shown in Figure 7, demonstrate that almost any reasonable waveform can be generated with high accuracy. This scheme is extremely robust, and is very insensitive to the frequency response of the membrane, or to changes in the frequency response of the membrane. Figure 7 shows that we successfully generated dual stroke waveforms with various amplitude and light-splitting ratios. In each case, the electrical signal sent to the speaker is very different from the membrane motion. We have also verified that in the 0 to $\approx 5kHz$ frequency range, the membrane shape is spherical and does not show "ripples" (this test is achieved by moving the laser spot on the surface of the membrane).

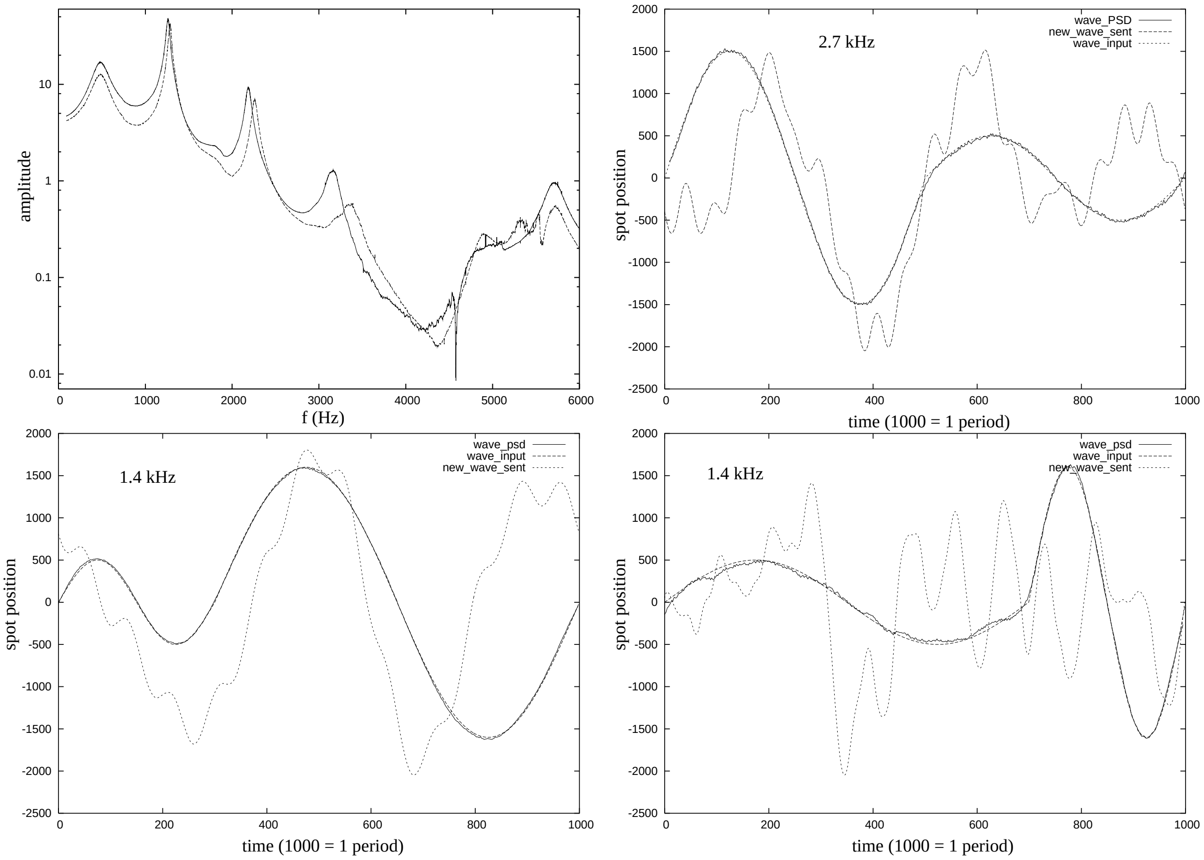

Fig. 7.— Vibrating membrane amplitude frequency response (top left): 2 measurements were taken about 10mn apart and show changes in the frequency response. Examples of membrane stroke profiles are given (top right, bottom left, bottom right): in each case, the long-dashed curve labeled "wave_input" is the desired stroke profile, the short-dashed curve labeled "new_wave_sent" is the actual electrical signal sent to the VM unit and the continuous curve labeled "wave_psd" is the membrane stroke as measured by the Position Sensing Device (PSD). In each case, there is a near-perfect match between the desired and obtained VM motions, but the electrical signal sent to the speaker greatly differs from these profiles.

5. Wavefront reconstruction

5.1. Simple Linear Control loop algorithm with dual-stroke curvature

The appropriate information needs to be extracted from each of the two virtual WFSs. Broadly speaking, low order aberrations should be computed from the WFS signal obtained during the "large stroke" ($+dz_2$ and $-dz_2$), while high order aberrations are extracted from the "small stroke" ($+dz_1$ and $-dz_1$) signals. Most importantly, high spatial frequency signals during the large stroke period should be ignored, as the defocus altitude likely exceeds both z_1 and z_2: these signals are now highly non-linear, and need to be rejected from the linear control loop. The simplest way to filter out this unwanted signals is to acquire a system response matrix where high spatial frequency signals are purposely erased from the "high stroke" period. This response matrix can then be inverted to produce a system control matrix using Singular Value Decomposition. With the two strokes scheme, the system response matrix is rectangular rather than square: if the number of actuators and the number of sensors are equal, the response matrix contains exactly twice as many curvature signals as there are actuators.

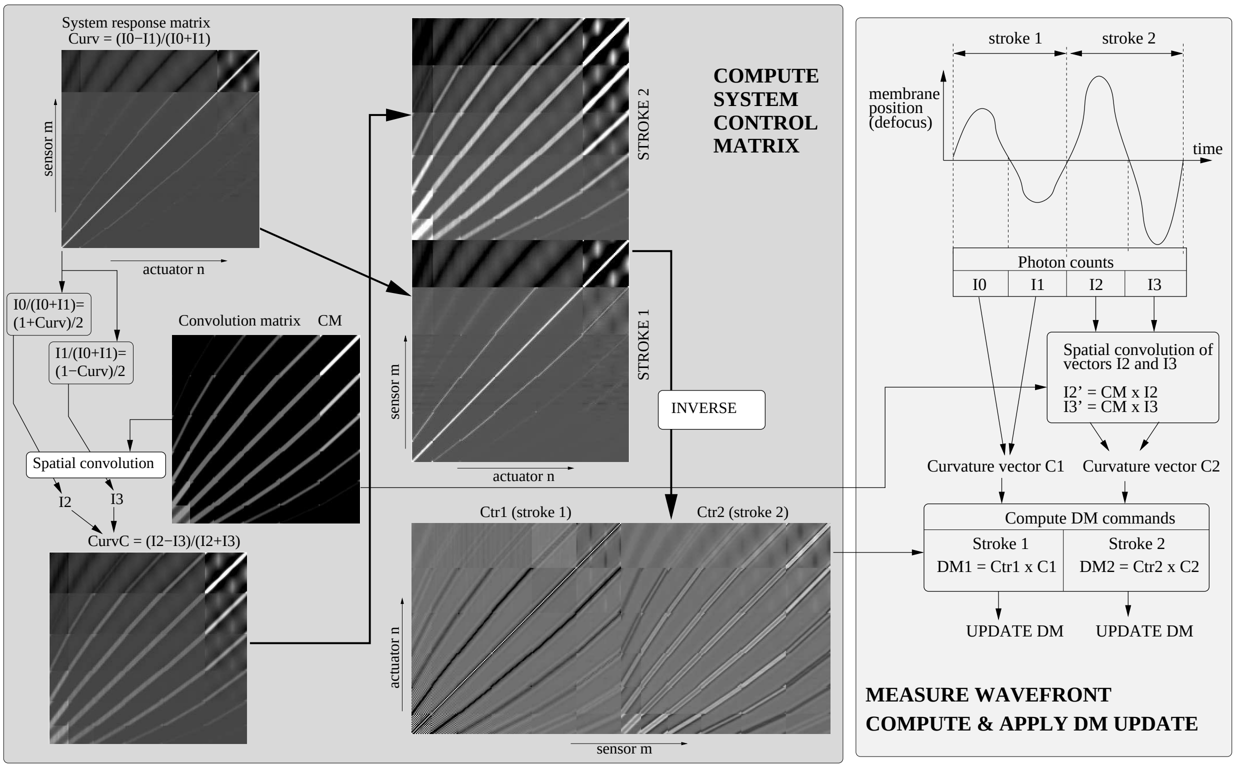

Fig. 8.— Control algorithm for dual stroke linear curvature wavefront sensing: system control matrix computation (left) and closed loop wavefront measurement/DM command computation (right). The control matrix is rectangular (there are more curvature measurements than DM actuators), and can be entirely computed from a single stroke system response matrix (top left, square matrix). To filter out the high spatial frequency information within stroke 2 measurement, the wavefront sensor intensity vectors measured during stroke 2 are spatially convolved (this is done by multiplying vectors I0 and I1 by a matrix). The same convolution is also used to generate the system control matrix. All matrices in this figure are shown for the 188 actuators Subaru Telescope curvature AO system.

For the high stroke half of the response matrix, filtering out high spatial frequencies is achieved by convolution of the photon count 2D pupil map by a "disk" kernel. As the membrane stroke increases, the size of this kernel also increases. Figure 8 shows how this is done by a matrix multiplication. With this scheme, the rectangular response matrix can be computed from a "standard" response matrix and an appropriately chosen kernel size.

The resulting control scheme is very similar to a conventional linear curvature system control algorithm. Photon counts from the wavefront sensors are used to compute a curvature vector, which is multiplied by the control matrix. The only difference is that the curvature vector is twice as long, and the control matrix is rectangular instead of square. In fact, it is preferable to split the matrix multiplication in two parts: as soon as the curvature vector from the first stroke (dz_1) is available, it is multiplied by the first half of the rectangular control matrix (which is square), and as soon as the second stroke (dz_2) is available, it is multiplied by the second half of the control matrix. The resulting algorithm is then identical to a standard curvature control algorithm with square matrices, except that the control matrices are swapped between each stroke.

5.2. Performance

A detailed simulation of single stroke and double stroke curvature systems has been performed

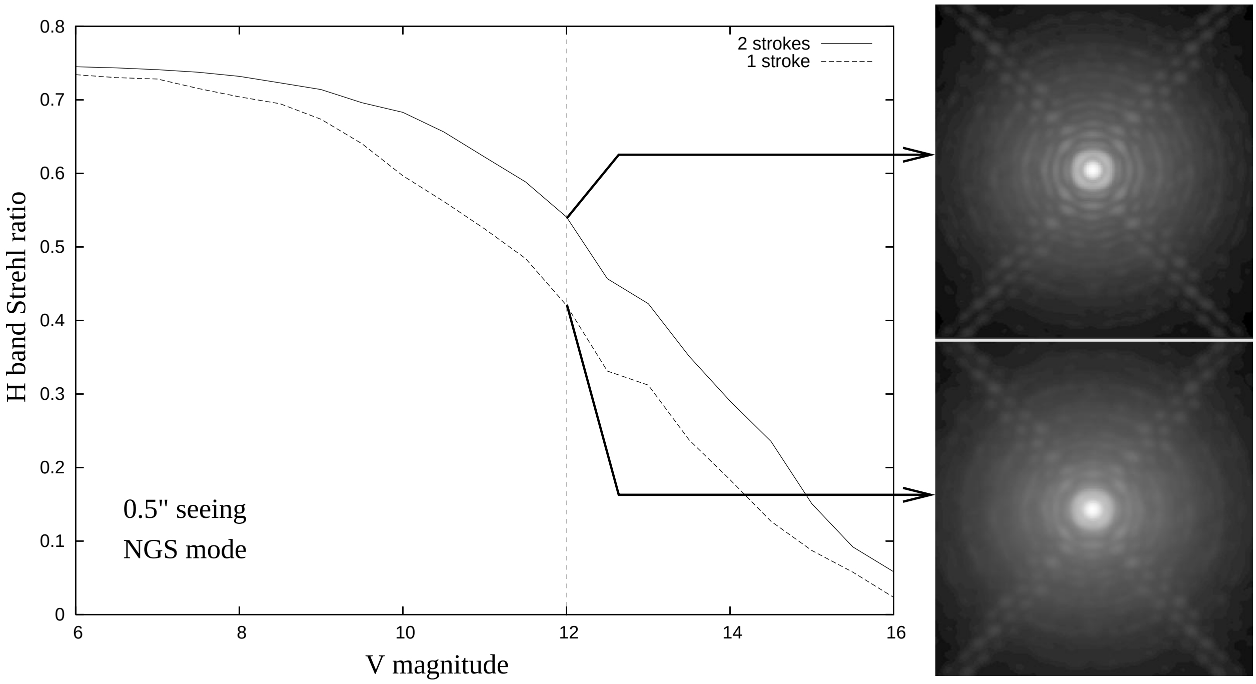

Fig. 9.— Simulated H-band Strehl ratio as a function of guide star magnitude in single and dual stroke modes. This simulation was performed for the 8.2m Subaru telescope 188-elements curvature AO system. With the dual stroke mode, a sensitivity gain of 1 to 1.5 stellar magnitude is achieved. Single and dual stroke PSFs obtained for a $m_V = 12$ star are shown on the right. The largest performance gain is obtained for intermediate to faint brightness guide stars: Strehl ration on bright stars is limited by the number of actuators in the system rather than wavefront sensor sensitivity.

to quantify the gain in performance between these two modes. The simulations assume a multilayer frozen flow for atmospheric turbulence, and include chromatic effects within the wavefront sensor. The pupil shape and diameter (8m), the wavefront sensor and bimorph deformable mirror geometries adopted for this simulation match the design of the Subaru Telescope 188 elements curvature AO system (see Guyon et al. (2004) for further details on this simulation). A direct comparison between the two modes is shown in Figure 9. We find that performance is optimal when $dz_2 \approx 3 \times dz1$, where dz_1 is very close to the optimal defocus distance which would be applied in single stroke mode. When Strehl ratio is used as a performance metric, at least a full stellar magnitude is gained in sensitivity by adopting the dual stroke scheme. As expected, the largest gain is obtained for low order aberrations (especially tip-tilt). Comparison between the PSFs obtained in single and dual stroke modes illustrates this gain in low order modes: the dual stroke PSF is crisper and shows higher contrast. The PSF obtained in the single stroke mode visually looks like the dual stroke PSF convolved by a “tip-tilt error kernel”. Reduction of low-order aberrations is especially beneficial for high dynamical range imaging at small angular separations, as coronagraphs are very sensitive to such aberrations.

For this simulation, we note that a fairly conventional control algorithm has been adopted (see §5.1) to maintain simplicity and avoid significant rework of the control loop software. Further gains are expected to be obtained from refinement of this linear control scheme (more optimal mode filtering between the two strokes, modal control, predictive control). By providing additional signals, the dual stroke scheme also comes with more “knobs” to tune, and a more thorough optimization of the control loop is likely to yield better performance.

6. Conclusions, Future work

The dual stroke wavefront sensing technique offers a significant performance gain over conventional "single stroke" curvature wavefront sensor. This sensitivity gain becomes larger as the number of actuators in the system increases. The technique is therefore expected to be especially attractive for Extreme-AO systems aiming at very high wavefront accuracy and for AO systems on large telescopes. We have shown in this paper that dual stroke curvature wavefront sensing can be implemented on existing curvature AO systems: the vibrating membrane traditionally used to produced the two defocused pupil image can be driven to produce four defocused images (it is therefore not necessary to build a separate wavefront sensor for the second defocus value), and the control algorithm for this new mode can re-use the linear matrix multiplication code currently used on curvature AO systems. On the 188 elements configuration adopted in this work, the overall sensitivity gain is 1 to 1.5 magnitude. The dual stroke scheme outlined in this paper will be implemented on the Subaru Telescope 188 actuators curvature AO system. Timing tests show that the necessary computations can be run at up to 3 kHz loop speed (6 kHz loop speed for single stroke), including data logging. The vibrating membrane used for this system is very similar to the one used for our laboratory test, which validated dual stroke membrane pattern at up to 3 kHz.

Further sensitivity improvement could be obtained by using a wavefront reconstruction algorithm which takes into account non-linear effects in the curvature wavefront sensor. For example, Tip-tilt may first be measured from the four defocused images, and these images can then be re-centered in the computer prior to computing higher order aberrations: this scheme would solve the non-linearity issue illustrated in Figure 3. More complex non-linear schemes could lead to much improved wavefront sensing sensitivity, and will be explored in an upcoming paper.

REFERENCES

Arsenault, R., Donaldson, R., Dupuy, C., Fedrigo, E., Hubin, N., Ivanescu, L., Kasper, M.E., Oberti, S., Paufique, J., Rossi, S., Silber, A., Delabre, B., Lizon, J., Gigan, P. 2004, Proc. SPIE, 5490, 47

Guyon, O., Arimoto, N., Blain, C., Colley, S., Eldred, M., Goto, M., Hattori, M., Hayano, Y., Iye, M., Kamata, Y., Kane, T., Kobayashi, N., Watanabe, M., Minowa, Y., Oya, S., Saito, Y., Takami, H., Takato, N. 2004, Proc. SPIE, 5490

Guyon, O. 2005, ApJ, 629, 592-614.

Racine, R. 2006, PASP, 118, 1066

Rigaut, F., Salmon, D., Arsenault, R., Thomas, J., Lai, O., Rouan, D., Véran, J.P., Gigan, P., Crampton, D., Fletcher, J.M., Stilburn, J., Boyer, C., Jagourel, P. 1998, PASP, 110, 152

Roddier, F. 1988, Appl. Opt., 27, 1223

Roddier, F., Northcott, M., Graves, J.E. 1991, PASP, 103, 131

Roddier, F. 1998, PASP, 110, 837

Takami, H., Takato, N., Hayano, Y., Iye, M., Oya, S., Kamata, Y., Kanzawa, T., Minowa, Y., Otsubo, M., Nakashima, K., Gaessler, W., Saint-Jacques, D. 2004, PASJ, 56, 225
